Bachelor Thesis

Parametric Study of Scaling Rules for a PEM Fuel Cell in Untethered Microrobots
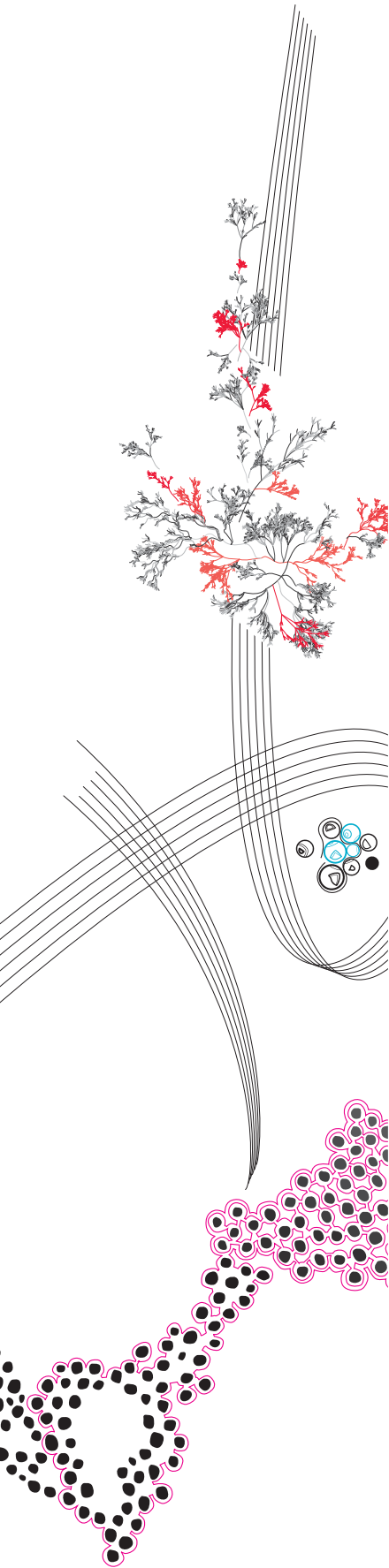
Astrid E. Hornman

Faculty of Engineering Technology
Department of Biomechanical Engineering

Chair: Dr. Arturo Susarrey Arce
Examination Committee:
Dr. Islam S.M. Khalil
Dr. Janset Dasdemir

October, 2023

UNIVERSITY OF TWENTE.

Abstract

Untethered Devices (UDs) can be defined as wireless devices within the millimetre range, and could have a significant impact on medicine. Some possible uses of microrobots include targeted drug delivery, treatment of vascular diseases, and cell delivery. In this paper a study is done on the effects of downscaling a UD that is powered by a PEM fuel cell. The effects of downscaling are tested for different inlet pressures and cell temperatures, as well as different flow plate designs. The parameters are tested within a range that is safe to use inside the human body. The result of this study shows that upon increasing pressure, the performance of the fuel cell increases. This is valid for all three sizes, thus this will also improve performance upon scaling down. In addition, the overall performance of the microrobot will improve upon scaling down, and also when the pressure is increased. Regarding the temperature, the performance of the microrobot will decrease upon increasing temperature. However, this difference in performance does become less significant for smaller sizes, thus this will likely become irrelevant upon scaling down further. Finally, different flow plate geometries have also been tested using a flow simulation. These show that a 5-step serpentine will result in the best performance of the fuel cell.

1   Introduction

Untethered Devices (UDs) or microrobots can be defined as wireless devices within the millimetre range, and could have a significant impact on medicine. An example of a UD is shown in Figure 1. Some possible uses of microrobots include targeted drug delivery [1], treatment of vascular diseases [2], and cell delivery [3]. Because they are small and wireless, they can reach places that existing medical devices cannot. UDs can shorten procedural time, and increase actuation precision, due to the lack of guidewires. As the amount of people with cardiovascular diseases is likely to increase, the need for better procedures increases as well, and thus researching and improving UDs can prove to be very valuable in the future. [4] Typically, these UDs move by deriving power from an externally applied magnetic field. However, there are several problems with this method. One of them includes the robustness of the setup, due to the need for strong magnets, which require cooling elements. Another is the dependence of distance between the magnets and the robot. This could be significantly different between patients, due to abdominal thickness or obesity. [6] An alternative solution to make these UDs move, is to have a power supply present on board the UD. A solution for this is a Proton
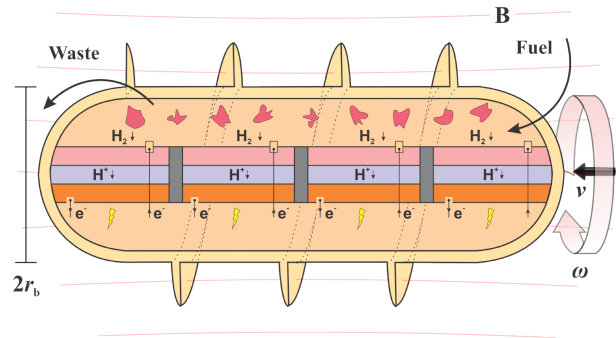

Figure 1: *Schematic of an Unthetered Device as used in the paper of Van Renselaar et al. B is the applied static magnetic field, r_b is the radius of the UD, ω is the angular velocity of the UD, v is the translational velocity of the UD. [5]*

Exchange Membrane (PEM) fuel cell. A schematic overview of a PEM fuel cell, can be seen in Figure 2. However, these are mostly applied on large scales and have yet to be used in sizes small enough to fit into the human body. To apply these PEM fuel cells into the UDs, they need to be sized down. Van Renselaar et al. [5] found that the efficiency increases when scaling down the UD and thus the fuel cells. To partly validate this model, a characterization of fuel cells upon scaling down will be done in this paper. Another important aspect that will be covered, is improving the output of the fuel cells, by finetuning certain parameters. The output needs to be optimized so that the fuel cell will eventually provide enough power for the operation of the robot. This optimization will also be tested upon scaling down.

As mentioned above, certain parameters can be finetuned to optimize the output of a PEM fuel cell. These parameters include gas pressure, operating temperature, flow plate geometry, hydrogen purity, gas humidification, and entrance geometry. [7, 8, 9, 10] Optimizing the output is defined as increasing the maximum amount of power derived from the fuel cell, as well as increasing the voltage output for a given current. According to Taccani and Zuliani
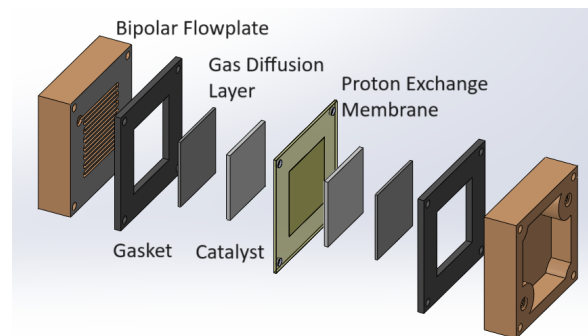

Figure 2: *Assembly of a PEM fuel cell with bipolar flow plates, a gasket, a gas diffusion layer, a catalyst, and a PEM.*

(a) *Flow plate geometry of the single serpentine*

(b) *Flow plate geometry of the 5-step serpentine*

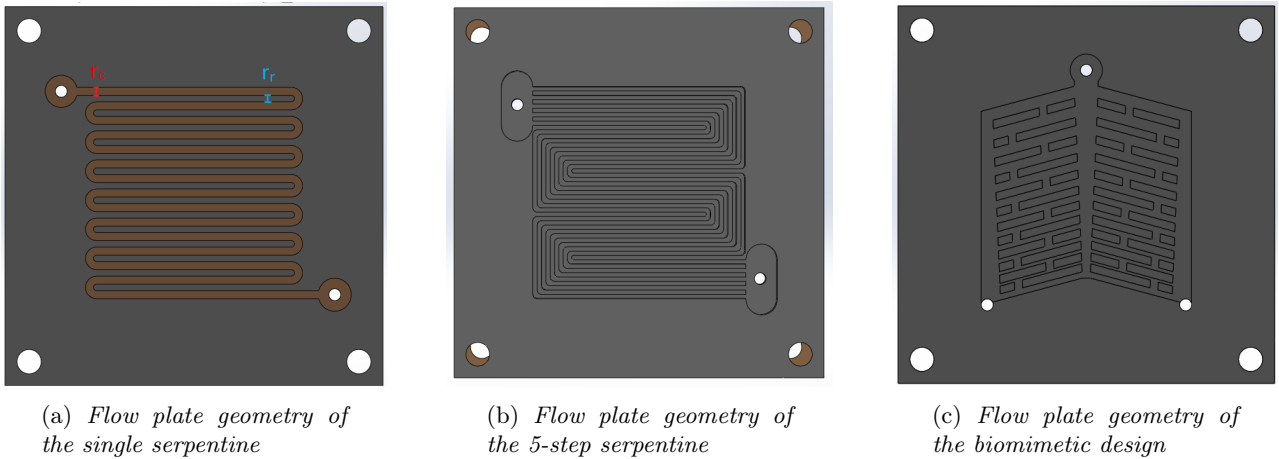(c) *Flow plate geometry of the biomimetic design*

Figure 3: *The three different flow plate geometries designed for the fuel cells. These are the designs for the medium size. Figure 3a shows the design of the flow plate with the single serpentine. Figure 3b shows the design for the 5-step serpentine. Figure 3c shows the design of the leaf-based flow plate.*

[11] increasing the anode side pressure will result in a significant performance increase. However, increasing the cell temperature will result in a performance decrease. Moreover, flow plate geometry will influence pressure drop, water management, temperature distribution, and distribution of gases, all these factors influence the output and durability of the fuel cell. [12, 13, 14] Furthermore, contaminated hydrogen will negatively affect the MEA (Membrane Electrode Assembly) in three different ways: the kinetic effect, the conductivity effect, and the mass transfer effect. All three of these phenomena will result in lower output from the fuel cell. [10] In addition, If the hydrogen gas is not humidified, the proton conduction will decrease, resulting in a lower output. [15] Finally, the entrance geometry will influence the gas distribution in the flow plate, thus affecting performance and durability. [9]

In this paper, several simulations will be done to test the effect of the abovementioned variables on a PEM fuel cell, within a range that can safely be used inside the human body. The model as proposed by Van Renselaar et al. [5] will be used and extended for this purpose. Extending it will be done by including various pressures and temperatures. In addition, three different flow plates will be designed and undergo a flow simulation, to test the effect of different inlet pressures. All these simulations will be done for three differently sized fuel cells to analyze the effects upon scaling down. The purpose of this is to be able to optimize the output of the PEM fuel cell more easily upon scaling down, so that eventually enough output can be generated to power the UD.

2   Methods

2.1   Model

In this paper, a UD with a PEM fuel cell is considered. Calcium hydride (CaH$_2$) is used to provide hydrogen to the fuel cell. The hydrogen flow produced by the calcium hydride is considered to be continuous at the anode side. The reactions that occur within the fuel cell at the anode and cathode side respectively, are as follows:

$$H_2 \quad \longrightarrow \quad 2H^+ + 2e^- \qquad (1)$$

$$O_2 + 4e^- + 4H^+ \quad \longrightarrow \quad 2H_2O \qquad (2)$$
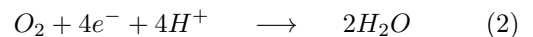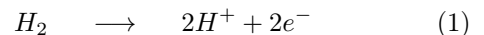
The calcium hydride provides the hydrogen at the anode side, which will be converted into protons and electrons, as shown in Equation 1. The protons will pass through the membrane, and the electrons through an external circuit, they will converge at the cathode side. At the cathode side Equation 2 will take place. Oxygen is taken from the air and combined with the protons and electrons to form water.

To calculate the potential of the fuel cell, the standard cell potential (E_e^0) has to be known. This can be calculated by $E_e^0 = E_C^0 - E_A^0$, where E_C^0 is the cathode potential and E_A^0 is the anode potential. Using the data from Van Renselaar et al. [5] this gives a standard cell potential of 1.23V. Using this value the Nernst potential (E_N) can be calculated, using Equation 3.

$$E_N = E_e^0 + \frac{RT}{nF} \ln \left(\frac{(P_{H_2})^2 P_{O_2}}{(P_{H_2O})^2} \right). \qquad (3)$$

In this equation, R is the gas constant, T is the temperature in Kelvin, n is the number of electrons transferred in one complete reaction ($n = 4$), F is Faraday's constant and P_x are the partial pressures of the gases.

However, in the fuel cell, certain voltage losses occur due to imperfections, an activation barrier and Ohmic resistance. This results in the following equation:

$$E_{MFC} = E_N - E_c - \frac{2RT}{n_A F} arsinh \left(\frac{I}{2I_0} \right) - R_e I$$
$$- cT \ln \left(\frac{I_L}{I_L - I} \right). \qquad (4)$$

In this equation, E_c is the crossover polarization, n_A is the number of electrons transferred at the anode side, I is the generated current, I_0 is the exchange current, R_e is the internal resistance of the fuel cell, and I_L is the limiting current. The parameter c can be empirically estimated. The values for these variables have all been determined experimentally, giving: $E_c = 0.96V, n_A = 2, I_0 = 3.19e^{-5}A, R_e = 0.33\Omega, I_L = 0.97A, c = 1,88e^{-4}$.[5]

Using Equation 4 the electrical power P_E can be calculated using Equation 5

$$P_E = E_{MFC}I. \tag{5}$$

Then Equations 4 and 5 can be used to make an I-V curve and a Power density plot.

The next step is to calculate the consumptionrates (C_x) of the three different substances: CaH_2, H_2O, and O_2. This can be done using Equation 6

$$C_x = \frac{Im_x}{2F\rho_x}, \tag{6}$$

where m_x is the molar mass of substance x and ρ_x is the density of substance x. Then Equations 5 and 6 can be used to derive a relation between power and consumption rate of CaH_2.

To incorporate the scaling rules into this model the size of the fuel cell as well as the size of the UD must be taken into account. Because when the UD becomes smaller, so does the fuel cell, as well as the drag and thus the required power. The electrical power will need to be converted to motion, this is done using tri-axial coils that create a dipole moment. When put into a static magnetic field the UD will rotate, and the geometry of the UD will ensure a motion in the desired direction. First, impedance-matching will need to occur to achieve maximum efficiency. This can be calculated using Equation 7.

$$R_w = \frac{E_{MFC}}{\pi J r_b^2} = \rho_w \frac{l_w}{\pi r_w^2}, \tag{7}$$

where J is the current density at maximum power, ρ_w is the resistivity of the wire material in the coils, l_w is the length of the wire, and R_w is the resistance of the tri-axial coil.

When the magnetic field is applied, a magnetic torque is generated, causing the UD to rotate. The flux changes in the coils will cause a back-EMF, and thus eventually a decrease in current. As a result, the effective current will be given by Equation 8.

$$I_{eff,i} = \pi r_b^2 J - \frac{2N_i BS_i \sin\phi_i \omega_i}{R_w}, \tag{8}$$

for i = 1,2,3,.... Where N_i is the number of turns of the ith coil, S_i is the surface area of the ith coil, ϕ_i is the angle of the ith electromagnetic coil with respect to a frame of reference, ω_i is the angular velocity of the UD around the axis of the ith coil, and B is the external magnetic field. This effective current is used in Equation 5.
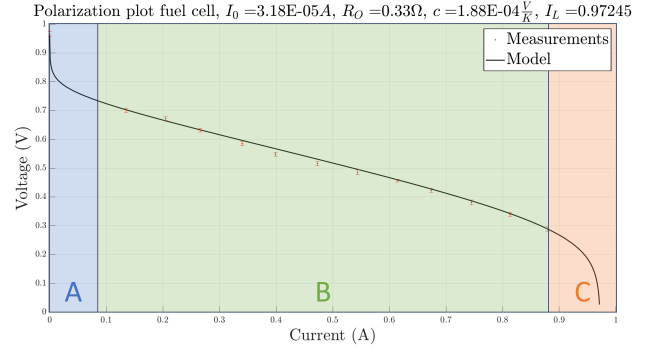

Figure 4: *Indication of the different characteristic regions within an I-V curve of a fuel cell. Region A indicates the activation region, Region B indicates the Ohmic region, and Region C indicates the Mass transport region. [17]*

To complete the rotational dynamics of the UD, the torque balance has to be computed. This should be done for low-Reynolds number where, $Re = \frac{2r_b\rho\|\mathbf{v}\|}{\eta}$ for a fluid with density ρ and viscosity η. This results in Equation 9.

$$NS\mathbf{I}_{eff} \times \mathbf{B} = 8\pi\eta r_b^3 \boldsymbol{\omega}. \tag{9}$$

Now by using Equation 5 and 8 the power can be related to the size. By including Equation 6 the consumption rates can also be related to size.

This model is used to simulate the response of the fuel cells to changing variables. The model has been used to test different pressures, of 1.0 bar, 1.5 bar, 2.0 bar, 2.5 bar, and 3.0 bar. This is based on the research done by Wang et al. [7] and Zeng et al.[16]. The response has been modelled and the three sizes of fuel cells are indicated in the figures. The response is characterized by the consumption rates, the I-V curve, the power density plot, and the power against the size. The power density is derived from the I-V curve using Equation 10.

$$P_E = \frac{VI}{A}, \tag{10}$$

where V is the voltage measured by the potentiostat, I is the current given by the potentiostat, and A is the active area of the fuel cell. A is related to r_b by $A = 2r_b^2$.

2.1.1 I-V Curve

Figure 4 shows the different characteristic regions of an I-V curve of a fuel cell. The first region, Region A, is called the activation region. The steep downward curve in this region is due to the activation energy needed for the electrochemical reactions on the catalytic surface. These reactions are shown in Equations 11 and 12 for the anode side.
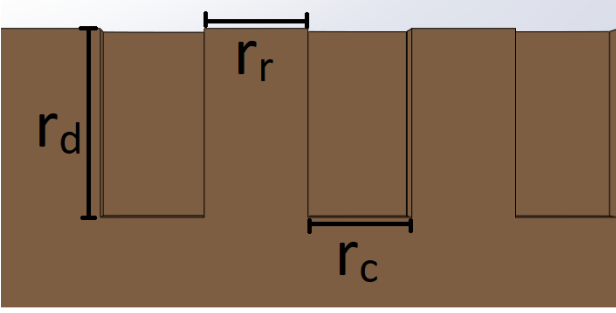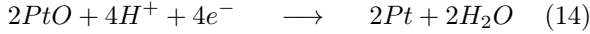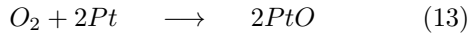
$$H_2 + 2Pt \longrightarrow 2PtH \tag{11}$$

$$2PtH \longrightarrow 2Pt + 2H^+ + 2e^- \tag{12}$$
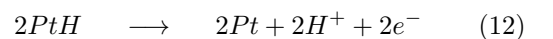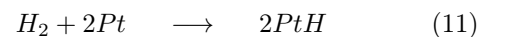
Figure 5: *Definitions of channel depth (r_d), rib width (r_r), and channel width (r_c).*

And Equations 13 and 14 show the reactions for the cathode side.

$$O_2 + 2Pt \quad \longrightarrow \quad 2PtO \qquad (13)$$

$$2PtO + 4H^+ + 4e^- \quad \longrightarrow \quad 2Pt + 2H_2O \quad (14)$$

The second region is the Ohmic region (Region B), here the current is limited by internal resistance (R_e in Equation 4) of the fuel cell. In this model this includes the resistance of the negative charge as well the resistance the H^+ cations encounter. This results in linear behaviour. The final region, is Region C and is called the Mass transport region. Here the voltage is limited by the mass transport limitations of the gases near the membrane, causing a pressure gradient. [17]

2.2 Simulation

First, the I-V curve and power density had to be derived to simulate the fuel cells for different pressures. These show how the fuel cell responds to different pressures. From these, the maximum power with corresponding current and voltage for each pressure was derived. Then these values were used in Equation 6 to calculate the consumption rates for each size, for varying pressures. This was then used to calculate the power against size for each pressure. Then a polyfit was applied to derive a relation between size and power. The same method has been used for various cell temperatures. The pressures have been adjusted in a range of 1.0 bar to 3.0 bar with steps of 0.5 bar. The cell temperatures that have been tested were: 273K, 283K, 293K, 300K, 310K.

2.3 Flow Plates

According to Taccani and Zuliani [11], Ruan et al. [12], and Manso et al. [13] the design of the flowplates also greatly influences the output of the fuel cells. Thus different flow plates have also been designed and tested for different pressures.

2.3.1 Designs

The different flow plate designs were chosen, based on the literature. The channel depth (r_d) for all flow

plates is 1mm. The first flow plate is shown in Figure 3a. Both the channel width (r_c) and rib width (r_r) are 1 mm and 0.8mm respectively, this is based on Manso et al. [13]. The second flow plate geometry is shown in 3b and is based on Taccani and Zuliani [11] and Manso et al. [13]. The channel and rib width are 0.55mm. The last flow plate geometry is a biomimetic design and is based on Ruan et al. [12], the design is shown in Figure 3c. The channel width ranges from 3mm to 0.35mm and is based on Murray's Law, which can be seen in Equation 15.

$$r^3 = r_1^3 + r_2^3, \qquad (15)$$

where r is the radius of the main channel, and r_1 and r_2 are the radii of the branched channels. This equation can be expanded to include any desired amount of branched channels. The relevant dimensions are shown in Figure 5

All medium-sized flow plates have a dimension of $47 \times 47mm$ with a flow field of $27 \times 27mm$, based on the medium-sized fuel cell. The dimensions for flow plates for the other fuel cells are scaled versions of these three designs. The dimensions are $36 \times 36mm$ with $16 \times 16mm$ for the smallest size and $55 \times 55mm$ with $35 \times 35mm$ for the largest. Table 1 summarises the most important dimensions of the flow plates.

2.3.2 Flow Simulations

To characterize the flow trajectories in the different flow plates, for different sizes, a flow simulation has been done, using Solidworks 2019. As preparation, a model 1/8-inch tube was also made. The tubes and plates were put into an assembly and all necessary preparations were done to perform the simulation. The inlet temperature varied from 1.5 bar to 3.0 bar with steps of 0.5 bar. The outlet pressure was set to 1.0 bar. The temperature was set to 293.2K, which is standard room temperature. This was done for all three flow plate designs and for all sizes. The flow trajectories are shown using arrows with a colour scale to indicate pressure differences. The surface parameters of the flow plates were also measured and used to calculate a pressure drop and a relative pressure drop. The pressure drop is defined as the difference between inlet pressure 1 and the outlet pressure,
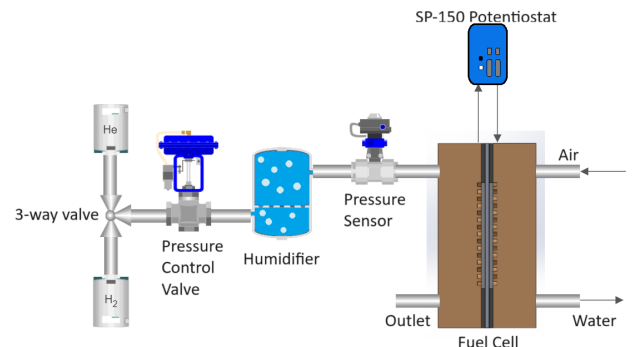

Figure 6: *Schematic overview of the setup for the experiments.*

Table 1: *Relevant dimensions of the nine different flow plates*

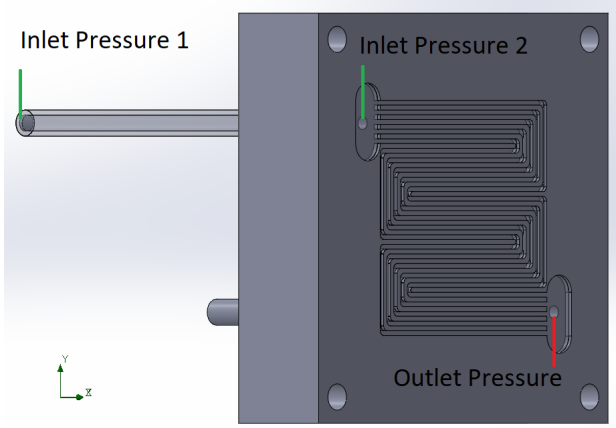|			Single Serpentine		5-Step		Leaf	
Size	**Dimensions**	**Active field**	**r_c**	**r_r**	**r_c**	**r_r**	**r_c**	**r_r**
Small	36mm x 36mm	16mm x 16mm	0.59mm	0.47mm	0.33mm	0.33mm	0.21mm-2.15mm	0.61mm
Medium	47mm x 47mm	27mm x 27mm	1mm	0.8mm	0.55mm	0.55mm	0.35mm-3mm	1mm
Large	55mm x 55mm	35mm x 35mm	1.3mm	1.04mm	0.71mm	0.71mm	0.46mm-4.11mm	1.3mm

Figure 7: *Definitions of inlet pressure 1, inlet pressure 2, and the outlet pressure.*

measured at the ports of the flow fields. The relative pressure drop is the pressure drop as a ratio of inlet pressure 1. All these results were plotted for all three designs and sizes and the surface parameters are clarified in Figure 7.

Fluid Dynamics Theory Due to friction in the channels a pressure drop will occur across the flow-plates, this can be calculated using the Darcy-Weisbach equation. [18] The Darcy-Weisbach equation is as follows

$$\frac{\Delta P}{L} = f * \frac{\rho}{2} * \frac{v^2}{D_H},\qquad(16)$$

where ΔP is the pressure drop, L is the length of the pipe in meters, D_H is the hydraulic diameter of the pipe in meters, ρ density of the gas in kg/m^3, v the average velocity of the gas in the pipe in m/s. f is the Darcy-Weisbach friction factor, which depends on the Reynolds number and the pipe roughness.

In the case of the flow plates, the length of the pipe, is the path length of the gas. This means that in the case of the 5-step serpentine, the length equals the length of one parallel channel, and not all channels put together. This also means that the pressure drop is calculated separately for each channel. In the case of the leaf geometry, the paths are not as straight-forward, but the pressure drop will still be calculated separately for each path.

The hydraulic diameter can be calculated using: $D_H = \frac{4A}{P}$, where P is the wetted perimeter. The wetted perimeter is the length of the wet part of the perimeter. In the case of the fuel cells, this is the entire circumference of the channel.

3 Results

The most important results of the experiments are shown in Figures 8 to 15. A complete overview of the results can be found in Appendix A.

3.1 Pressure variations

Figures 8 and 9 show the most important results of the pressure simulations.

Figure 8 shows the consumption rate of CaH$_2$ for different UD sizes, indicated by the vertical lines. This graph shows that there is a non-linear relation between the size of the UD and the consumption rate.

In Figure 9a the increase in consumption rate for the different pressures, across the different sizes is depicted more clearly. Here it can be seen that the percentage increase in consumption rate is very similar for all three UD sizes and within a range of 100% to 102%. In Figure 9b the increase in maximum output power is depicted for all three sizes. This also shows a similar percentage increase for all three sizes and within a range of 100% to 104%.

Subsequently, Figure 9c shows the power density plot for the different pressures. From this it becomes clear that the maximum output power increases the most, and for other current densities the increase is mostly insignificant.

In addition, Figure 9d shows the I-V curve for the different pressures. From this it can be seen that the most significant change takes place in the Ohmic region. The Activation and Mass Transport region remain almost unchanged.

Finally in Figure 9e shows the relation between the UD size, and thus the fuel cell size, and the maximum output power. The sizes of the fuel cells have been indicated with markers. From this graph, it becomes clear that this is a non-linear relation.

3.2 Temperature variations

Figures 10 and 11 show the most significant results of the temperature simulations.

Figure 10 shows the relation between the consumption rate of CaH$_2$ and UD size for different temperatures. The UD sizes corresponding to the three different fuel cell sizes are indicated with vertical lines. From this graph, it becomes clear that there is a non-linear relation.

In addition, Figure 11a highlights the differences in consumption rate for the different temperatures. From this, it can be seen that there is a decrease in
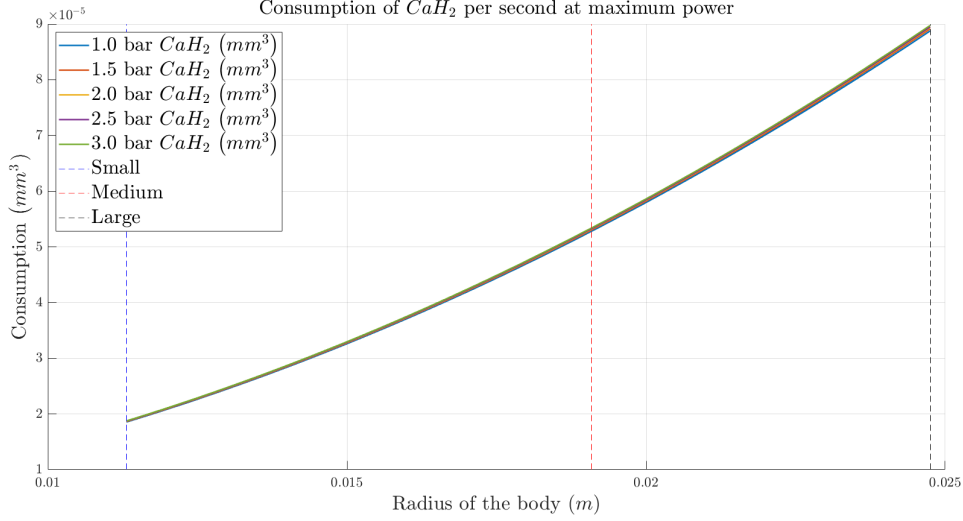
Figure 8: *Different consumption rates of CaH_2 for different pressures. Sizes for the fuel cells are indicated by the vertical lines.*

consumption rate for increasing temperature. This percentage decrease is very similar for all three sizes and within a range of 100% to 95%.

Furthermore, Figure 11b shows the decrease in maximum output power for the different temperatures, across all three sizes. It can be seen that the percentage difference for the maximum output power is also very similar across the different sizes, this is in a range of 100% to 90%.

Subsequently, Figure 11c shows the decrease in output power, and it can be seen that the decrease is most significant for the maximum output power.

Figure 11d shows the I-V curve for the different temperatures. Here it can be seen that the decrease is most significant in the Ohmic region and that the other two regions remain almost unchanged.

Lastly, Figure 11e shows the relation between UD size, and also the corresponding fuel cell sizes, and the maximum output power. Similar as for pressure it can be seen that this does not result in a linear relation.

3.3 Flow simluations

Figure 12 shows the flow trajectories of the single serpentine flow plate for inlet pressures ranging from 1.5 bar to 3.0 bar. All inlet pressures give a pressure drop that results in an outlet pressure of roughly 90000.00 Pa. The highest inlet pressure gives the largest pressure drop.

In Figure 13 the flow trajectories of the 5-step flow plate are shown. When comparing these to the single serpentine it can be seen that there are still pressure drops, however they are significantly smaller than those in the single serpentine.

In addition, Figure 14 shows the flow trajectories of the leaf geometry flow plate. It can be seen that these have relatively low pressure in the entire plate, on the other hand, they have a low pressure drop in

comparison to the other plates.

Finally, Figure 15 shows the percentage pressure drop between inlet pressure 1 and the outlet pressure, for the three different sizes. It can be seen that for the small size, the leaf has the smallest pressure drop in a range of 25% to 55%, and increases for increasing pressure. The single serpentine has the largest pressure drop in the range of 30% to 68%. For the medium size, the leaf is still the smallest with a range of 18% to 40%, and the single serpentine the largest with 30% to 68%. Lastly, for the largest size, the leaf remains the smallest with a range of 18% to 40% and the single serpentine the largest with 34% to 68% From this, it can be seen that the leaf geometry has the smallest pressure drop and the single serpentine the largest. This remains the same for all three sizes, however the differences between the geometries do become smaller, when the size is decreased. This is because of the fact that the leaf geometry increases in pressure drop as the size decreases.

## 4 Discussion

4.1 Pressure variations

Figure 8 shows a non-linear relation between UD size and consumption rate of CaH_2. It can be seen that as the UD size becomes smaller, the consumption rate of CaH_2 to reach maximum power decreases. Furthermore, the relation is quadratic. This means that as the UD size increases, the consumption rate increases at an accelerating rate. However, when the UD size decreases, the consumption rate decreases at a decelerating rate. This means that upon scaling down of the UD, the consumption rate of CaH_2 will decrease however, at some point the difference in consumption rate of CaH_2 could become insignificant. Yet, the fact that the consumption rate decreases with UD size is still a good prospect for the creation of microrobots.
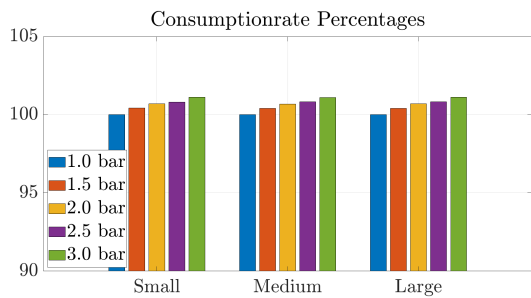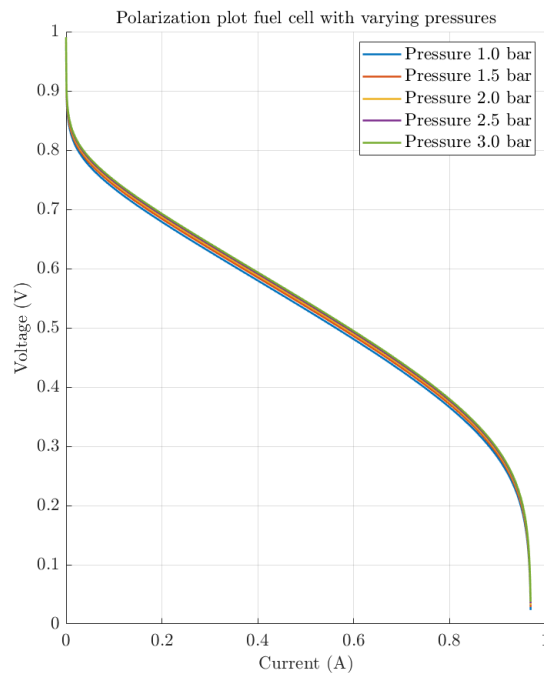
(a) *Values for the consumption rate of CaH_2 normalized against the values for 1.0 bar pressure, plotted for the three different sizes*
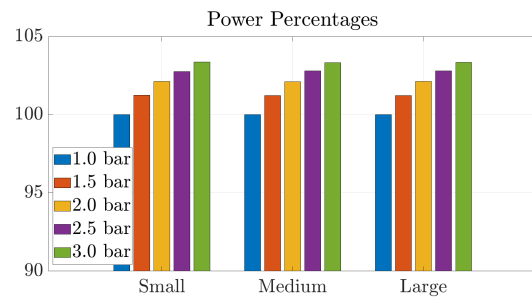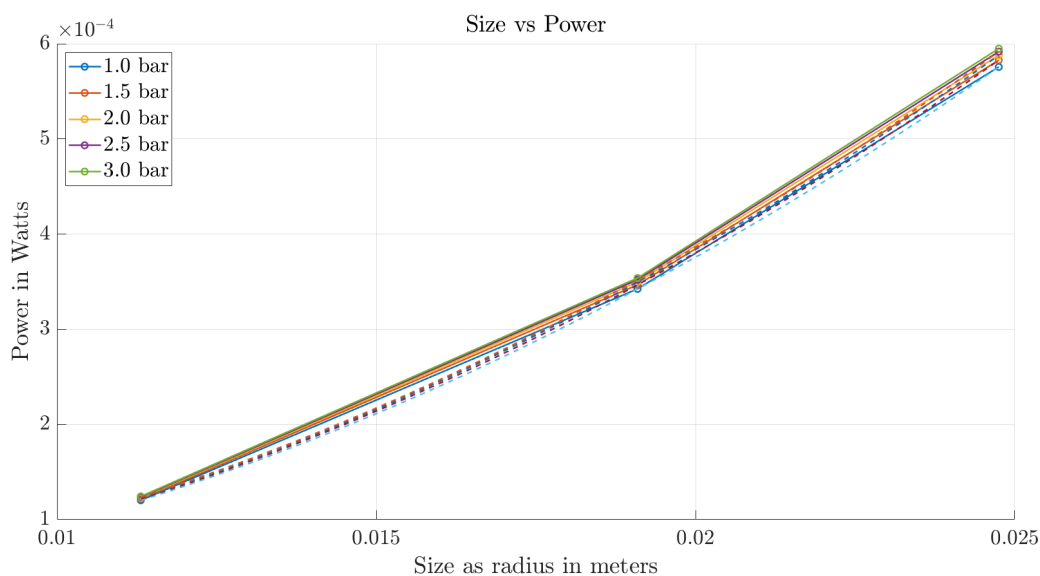

(b) *Values for the maximum power output normalized against the values for 1.0 bar pressure, plotted for the three different sizes*
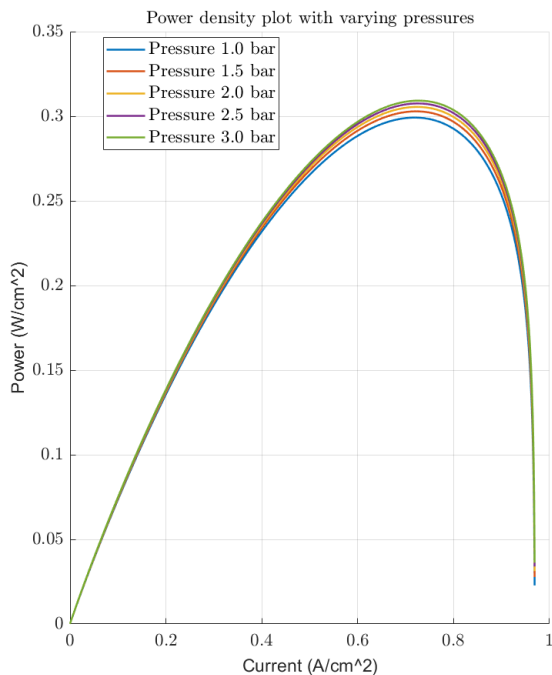
(c) *Power density plot for the varying pressures.*

(d) *I-V curve for the varying pressures.*

(e) *Power related to different sizes of fuel cells relative to UD size. A polyfit has also been applied for each of the different pressure variations. The three different sizes of the fuel cells have been marked with an 'o'.*

Figure 9: *Results of the pressure variation experiments. Based on the model proposed by Van Renselaar et al. [5]*
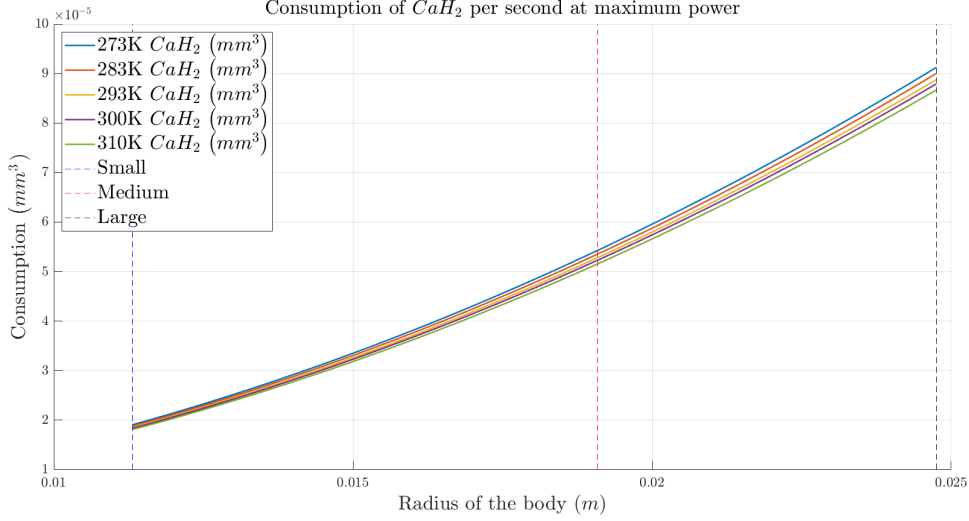
Figure 10: *Different consumption rates of CaH_2 for different temperatures. Sizes for the fuel cells are indicated by the vertical lines.*

Because, as the UD decreases, the amount of fuel that can be onboard will also decrease. However it would have been more favourable if the consumption rate of CaH_2 would decrease at an accelerating rate.

Figure 9a shows the percentage increase of consumption rate of CaH_2 for increasing pressures. For the pressure range of 1.0 bar to 2.5 bar, it appears that when the pressure increases, the step size for the percentage increase becomes smaller. However, between 2.5 bar and 3.0 bar the step size is suddenly larger than expected. The former would mean that increasing pressure could have a square root relation and would result in a limited increase of the consumption rate of CaH_2. While the latter would mean that there could be a positive linear relation between pressure and consumption rate of CaH_2 and thus seemingly unlimited.

When looking at Figure 9b it can be seen that as the pressure increases, the maximum output power increases as well. There also appears to be a square root relation between the increasing pressure and the maximum output power. This means that as the pressure increases, the step size of the percentage output power becomes smaller and eventually reaches a limit. For the UD this means that increasing the pressure will have limited benefits for the maximum power output.

When the results of Figures 9a and 9b are combined it becomes clear that the percentage power increase is larger than the increase in consumption rate of CaH_2 and could thus be beneficial for the eventual microrobot. In addition, if the relation between consumption rate and pressure, is square root, then the relation between consumption rate and power will be linear. However, if the relation between pressure and consumption rate of CaH_2 is linear, then consumption rate will increase at a constant rate, while the power will increase at a decelerating rate. Thus the latter will be less favourable for the microrobot than

the former. When plotting the consumption rate of CaH_2 against the maximum output power, it can be seen that this results in a linear relation and thus the more favourable scenario.

In addition Figures 9a and 9b show that the relations for pressure and consumption rate, and pressure and maximum output power, are the same for all three sizes. For the scaling rules, this means that upon scaling down, the same percentage increase of consumption rate and ouput power is expected.

Then, when analyzing Figure 9d, it shows that the voltage output increases for a given current, when the pressure is increased. More precisely, the Ohmic region and the Mass transport region of the I-V curve show improvements. This means that due to the higher pressure the internal resistances within the fuel cell decrease, as well as the mass transport limitations. In addition, this indicates that not just the performance of the UD itself, but also the performance of the fuel cell improves when the pressure is increased. The same effect becomes clear in Figure 9c, as the power increases with the pressure for a given current. However, the maximum power increases the most. In contrast, powers for other currents increase less, indicating that the result is best when the fuel cell operates at a current that corresponds to the maximum power.

Furthermore, Figure 9e shows that as the UD size decreases, the maximum ouput power decreases at a decelerating rate. This means that as UD size becomes smaller the output power will near a limit. This is a favourable result for the UD, as scaling down the UD will result in an increasingly smaller power drop. Thus, a very small UD could produce almost the same amount of power as a slightly larger one, while it will need less power to move as the negative forces acting on it, such as drag, will become less.
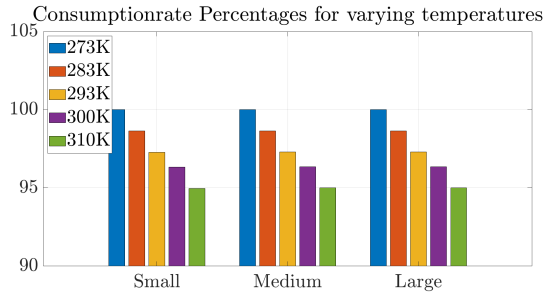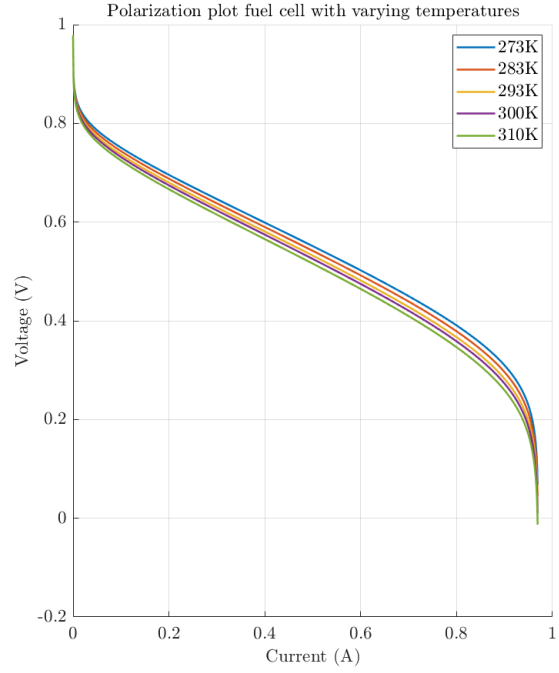
(a) *Values for the consumption rate of CaH_2 normalized against the values for 273K cell temperature, plotted for the three different sizes*
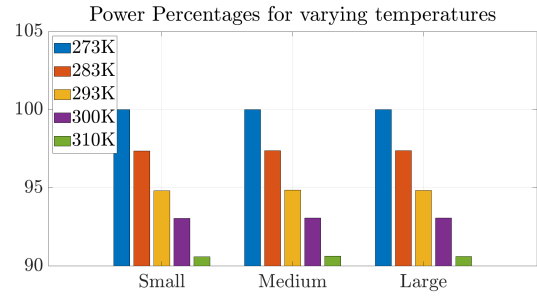
(b) *Values for the maximum power output normalized against the values for 273K cell temperature, plotted for the three different sizes*
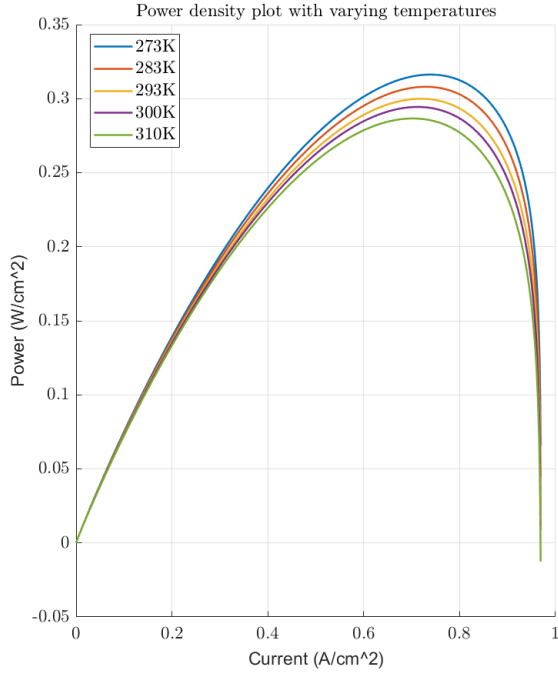
(c) *Power density plot for the varying temperatures.*

(d) *I-V curve for the varying temperatures.*
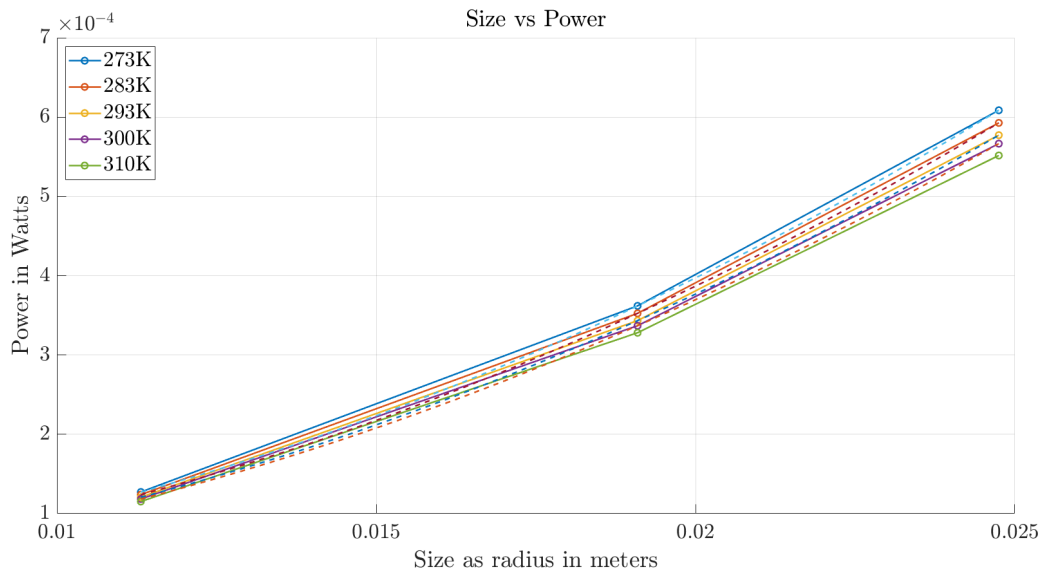
(e) *Power related to different sizes of fuel cells relative to UD size. A polyfit has also been applied for each of the different temperature variations. The three different sizes of the fuel cells have been marked with an 'o'.*

Figure 11: *Results of the temperature variation experiments. Based on the model proposed by Van Renselaar et al. [5]*

(a) *Flow in the medium single serpentine plate with 1.5 bar pressure.*

(b) *Flow in the medium single serpentine plate with 2.0 bar pressure.*

(c) *Flow in the medium single serpentine plate with 2.5 bar pressure.*

(d) *Flow in the medium single serpentine plate with 3.0 bar pressure.*
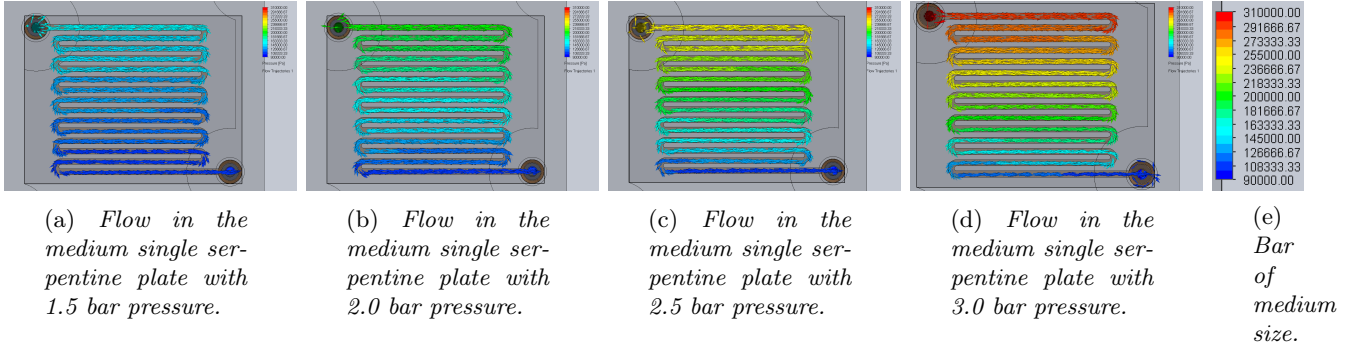
(e) *Bar of medium size.*

Figure 12: *Flow simulation results of the medium-sized single serpentine flow plate with varying pressures. Temperature is set to 293.20K and static pressure to 101325.00 Pa. Colour scale bar is set to 310000.00 Pa (red) to 90000.00 Pa (blue). Figure 12e shows the colour scale bar corresponding to the simulations.*

4.2 Temperature variations

When analysing the results for the temperature variations, it can be seen that the performance decreases when the temperature increases. This corresponds to the experiments done by Wang et al. [7], where they tested cell temperature and humidification.

Figure 10 shows the same relation between consumption rate of CaH_2 and UD size as Figure 8.

When analysing Figure 11a there appears to be an inverse-square relation between consumption rate and temperature. This means that as the temperature increases, the consumption rate will reach a lower limit. For the microrobot, it is beneficial that the consumption rate of CaH_2 is decreased by an increasing temperature. Nevertheless, there is a lower limit to the consumption rate, however for applications inside the human body there are safety limits as to the maximum cell temperature, thus the lower limit cannot be reached.

Figure 11b shows an inverse-square relation between the maximum output power and temperature. This implies a decelerating negative effect on the maximum output with increasing temperatures. Thus, this will also reach a lower limit.

When combining Figures 11a and 11b a linear relation between the consumption rate of CaH_2 and maximum output power becomes visible again. This

is expected, as changing the cell temperature instead of the inlet pressure should not have an effect on the nature of this relation.

When looking at Figure 11c it can be seen that the effect of cell temperature is most significant when operating at maximum power. In addition, the decrease in performance in the Ohmic region of the I-V curve in Figure 11d, can be explained by the fact that the membrane in the fuel cell acts as a conductor to the protons. For conductors, it goes that as the temperature increases, so does the resistance. Thus, a higher temperature increases the membrane's resistance to protons, thus increasing the internal resistance, thus decreasing the voltage. For the Mass transport region, the decrease in voltage upon increasing pressure can be explained by the fact that the diffusivity of the membrane increases, thus cross-over of O_2-gas and H_2-gas can happen more easily, which results in a decrease of performance.

Finally, looking at Figure 11e it can be seen that similarly to Figure 9b the maximum output power will eventually reach a lower limit. However, a clear difference between the two graphs is the larger effect of temperature increase when compared to the pressure increase. The different graphs divert significantly more for different temperatures than for different pressures.
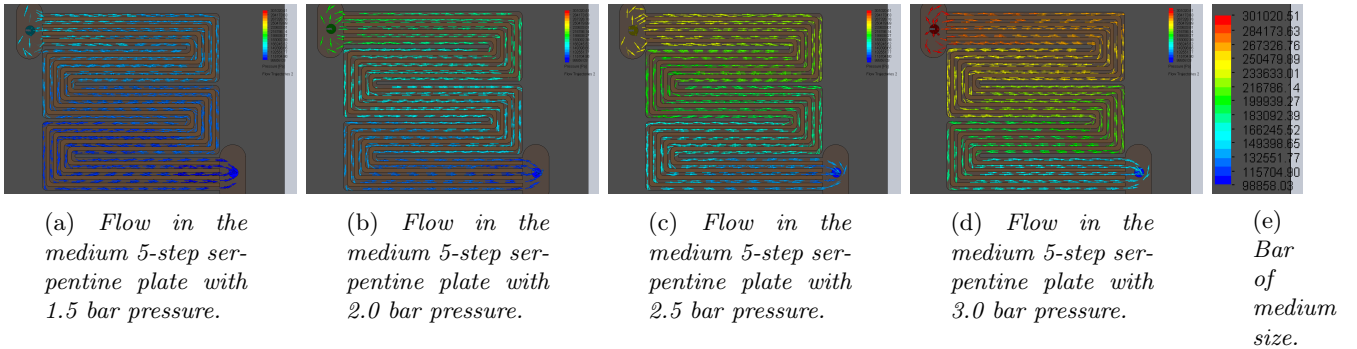

(a) *Flow in the medium 5-step serpentine plate with 1.5 bar pressure.*

(b) *Flow in the medium 5-step serpentine plate with 2.0 bar pressure.*

(c) *Flow in the medium 5-step serpentine plate with 2.5 bar pressure.*

(d) *Flow in the medium 5-step serpentine plate with 3.0 bar pressure.*

(e) *Bar of medium size.*

Figure 13: *Flow simulation results of the medium-sized 5-step serpentine flow plate with varying pressures. Temperature is set to 293.20K and static pressure to 101325.00 Pa. Colour scale bar is set to 301020.51 Pa (red) to 98858.03 Pa (blue). Figure 13e shows the colour scale bar corresponding to the simulations.*
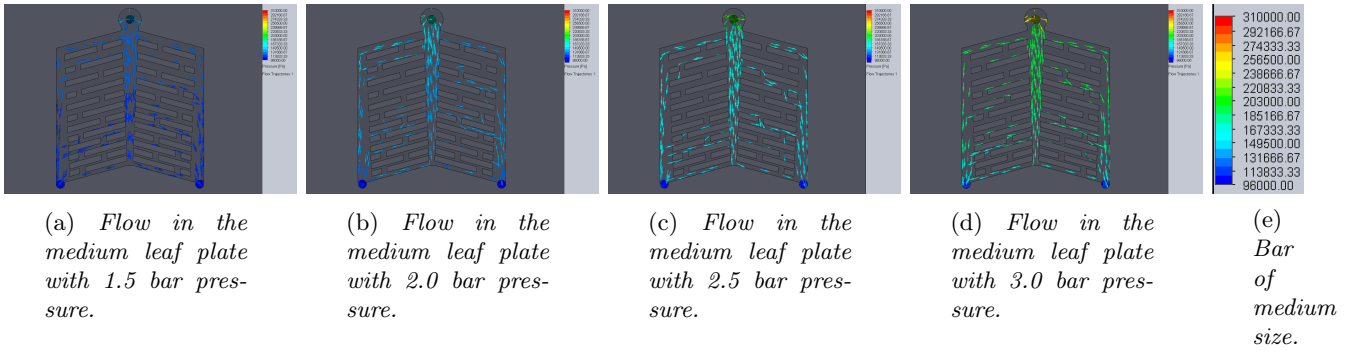
(a) *Flow in the medium leaf plate with 1.5 bar pressure.*

(b) *Flow in the medium leaf plate with 2.0 bar pressure.*

(c) *Flow in the medium leaf plate with 2.5 bar pressure.*

(d) *Flow in the medium leaf plate with 3.0 bar pressure.*

(e) *Bar of medium size.*

Figure 14: *Flow simulation results of the medium-sized leaf flow plate with varying pressures. Temperature is set to 293.20K and static pressure to 101325.00 Pa. Colour scale bar is set to 310000.00 Pa (red) to 96000.00 Pa (blue). Figure 14e shows the colour scale bar corresponding to the simulations.*

4.3   Flow Simulations

Furthermore, the flow trajectories of the flow plates have also been simulated. These results can be seen in Figure 12 to Figure 14. When the different geometries are compared, it becomes clear that the single serpentine gives the largest pressure drop, then the 5-step, and finally the leaf gives the smallest pressure drop. However, when Figure 23 is also included in this analysis, it can be seen that the leaf does indeed provide the lowest pressure drop, yet it also provides the lowest pressure overall. This is most likely caused by the large pressure drop that happens at the inlet of the flow field. Therefore, the difference between the inlet and outlet pressure is small, but there is a large difference between the applied pressure of 3.0 bar at inlet 1 and the outlet pressures of the leaf geometry. And as discussed before, Figures 9c and 9d show that a higher pressure results in a better performance. Thus, even though the leaf geometry results in the smallest pressure drop, it is most likely not the best geometry to use for optimisation purposes. This means that the 5-step serpentine, will most likely be the best geometry to use. Considering that it provides a smaller pressure drop than the single serpentine, but still has a relatively high overall pressure in comparison to the leaf geometry.

Then when the different pressures for each geometry are compared, it becomes clear that each inlet pressure results in roughly the same outlet pressure, and thus that a higher inlet pressure, results in a larger pressure drop. This also means that a lower inlet pressure results in a better pressure distribution, which could yield more favourable results where durability is concerned. Because a more equal pressure distribution, means that the membrane wears out equally for the entire area, whereas an inconsistent distribution, will lead to certain parts, in this case, the top, will wear out faster than the bottom and might lead to a shorter lifespan in general. However, a higher pressure might still be more favourable for the performance, thus a trade-off will have to be made, based on functional priority.

In addition when looking at Figure 15 it turns out that the differences in pressure drop become smaller when the fuel cell size decreases. This could indicate that when the fuel cells are sized down even further, the pressure drop might not significantly differ per design. In that case, the design can be chosen, based only on the pressure distribution.

As mentioned in Section 2.3.2 the pressure drop depends on the density, flow velocity, the Darcy-Weisbach friction coefficient, the length and the hydraulic diameter. In the conducted experiments the density, flow velocity and friction were kept constant. Thus the variations in pressure drop result from variations in the length and hydraulic diameter. As the length of the channels increases, the pressure drop
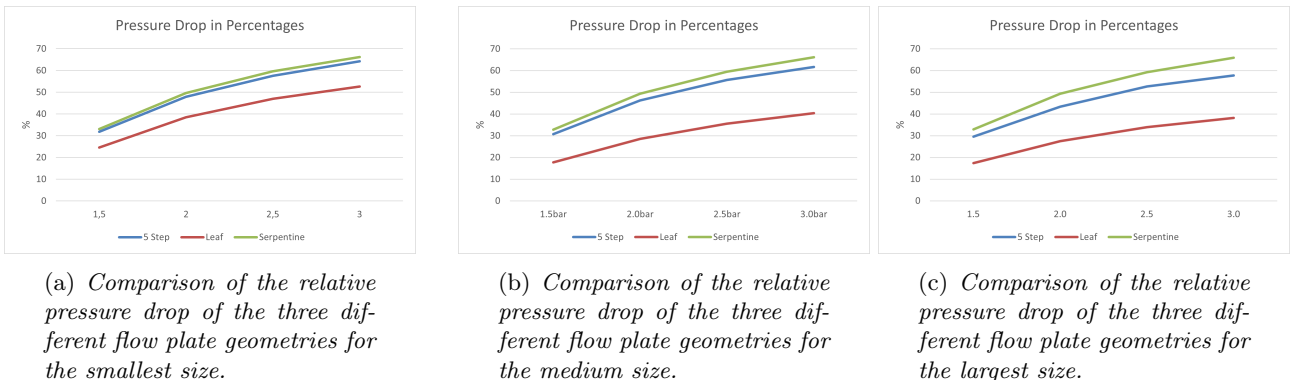

(a) *Comparison of the relative pressure drop of the three different flow plate geometries for the smallest size.*

(b) *Comparison of the relative pressure drop of the three different flow plate geometries for the medium size.*

(c) *Comparison of the relative pressure drop of the three different flow plate geometries for the largest size.*

Figure 15: *Results of surface parameter analysis of the flow simulations with varying pressures.*

also increases, and the single serpentine has a longer length than the 5-step, which thus results in a larger pressure drop. The leaf geometry has the shortest pathlength, and thus the lowest pressure drop. In addition, when the hydraulic diameter increases, the pressure drop will decrease. And the hydraulic diameter is increased, by decreasing the wetted perimeter, but increasing the cross-sectional area. Because, the depth/width-ratio is different for the different geometries, this can explain additional differences in pressure drop. To decrease the pressure drop, certain changes in channel geometry can be made, for example changing the depth/width-ratio, using a sloped channel, using a trapezoid cross-section instead of square and rectangle shapes.

For further research it is recommended that the flow plates are produced and tested as a complete fuel cell, to validate the outcomes of the simulations. In addition, the geometry of the channels of the 5-step serpentine can be changed and tested in simulations to try to reduce the pressure loss, and create a better distribution. The complete fuel cells will also need to be tested with the simulated inlet pressures and cell temperatures, to confirm the model and simulations. This will need to be done for the three sizes of this paper. Finally, even smaller sizes will need to be simulated and tested to reach the goal of a UD that can be inserted into the human body.

This will need to be done for the three sizes of this paper. Finally, even smaller sizes will need to be simulated and tested to reach the goal of a UD that can be inserted into the human body.

5   Conclusion

In this paper, the scaling rules of an Unthetherd Device (UD) have been modelled and tested for different inlet pressures and cell temperatures. The model proposed by Van Renselaar et al. [5] has been extended to include these variables. These variables have been modelled using three different sizes of UDs and PEM fuel cells.

It has been found that increasing the pressure improves the performance of the fuel cell. The maximum output power will most likely reach a lower limit, for smaller sizes, thus scaling down of the UD will be beneficial, as drag will continue to decrease. In addition, increasing the temperature decreases the performance of the UD. However, this decrease will also reach a lower limit, thus for very small sizes, this will most likely not be a problem.

Where flow plate geometry is concerned, the 5-step serpentine will most likely result in the best performance of the fuel cell, as it provides the highest pressure and the best pressure distribution.

For further research it is recommended that the flow plates are produced and tested as a complete fuel cell, to validate the outcomes of the simulations. In addition, the geometry of the channels of the 5-step serpentine can be changed and tested in simulations to try to reduce the pressure loss, and create a better distribution. The complete fuel cells will also need to be tested with the simulated inlet pressures and cell temperatures, to confirm the model and simulations.

References

[1] Deasung Jang et al. "Targeted drug delivery technology using untethered microrobots: a review". In: *J. Micromech. Microeng.* 29.5 (Mar. 2019), p. 053002. ISSN: 0960-1317. DOI: 10.1088/1361-6439/ab087d.

[2] Semi Jeong et al. "Penetration of an artificial arterial thromboembolism in a live animal using an intravascular therapeutic microrobot system". In: *Med. Eng. Phys.* 38.4 (Apr. 2016), pp. 403–410. ISSN: 1350-4533. DOI: 10.1016/j.medengphy.2016.01.001.

[3] Pelin Erkoc et al. "Mobile Microrobots for Active Therapeutic Delivery". In: *Adv. Therap.* 2.1 (Jan. 2019), p. 1800064. ISSN: 2366-3987. DOI: 10.1002/adtp.201800064.

[4] Junsun Hwang, Jin-young Kim, and Hongsoo Choi. "A review of magnetic actuation systems and magnetically actuated guidewire- and catheter-based microrobots for vascular interventions". In: *Intel. Serv. Robotics* 13.1 (Jan. 2020), pp. 1–14. ISSN: 1861-2784. DOI: 10.1007/s11370-020-00311-0.

[5] Erwin van Renselaar et al. "Scaling Rules for Microrobots with Full Energetic Autonomy". In: *2022 International Conference on Manipulation, Automation and Robotics at Small Scales (MARSS)* (July 2022), pp. 1–6. DOI: 10.1109/MARSS55884.2022.9870509.

[6] Nabil Simaan, Rashid M. Yasin, and Long Wang. "Medical Technologies and Challenges of Robot-Assisted Minimally Invasive Intervention and Diagnostics". In: *Annu. Rev. Control Rob. Auton. Syst.* 1.1 (May 2018), pp. 465–490. ISSN: 2573-5144. DOI: 10.1146/annurev-control-060117-104956.

[7] Lin Wang et al. "A parametric study of PEM fuel cell performances". In: *Int. J. Hydrogen Energy* 28.11 (Nov. 2003), pp. 1263–1272. ISSN: 0360-3199. DOI: 10.1016/S0360-3199(02)00284-7.

[8] Faysal Tiss, Ridha Chouikh, and Amenallah Guizani. "Dynamic modeling of a PEM fuel cell with temperature effects". In: *Int. J. Hydrogen Energy* 38.20 (July 2013), pp. 8532–8541. ISSN: 0360-3199. DOI: 10.1016/j.ijhydene.2012.09.101.

[9] Wei-Hsin Chen et al. "Geometry optimization and pressure analysis of a proton exchange membrane fuel cell stack". In: *Int. J. Hydrogen Energy* 46.31 (May 2021), pp. 16717–16733. ISSN: 0360-3199. DOI: 10.1016/j.ijhydene.2021.01.222.

[10] Xuan Cheng et al. "A review of PEM hydrogen fuel cell contamination: Impacts, mechanisms, and mitigation". In: *J. Power Sources* 165.2 (Mar. 2007), pp. 739–756. ISSN: 0378-7753. DOI: 10.1016/j.jpowsour.2006.12.012.

[11] Rodolfo Taccani and Nicola Zuliani. "Effect of flow field design on performances of high temperature PEM fuel cells: Experimental analysis". In: *Int. J. Hydrogen Energy* 36.16 (Aug. 2011), pp. 10282–10287. ISSN: 0360-3199. DOI: 10.1016/j.ijhydene.2010.10.026.

[12] Hanxia Ruan et al. "Design and simulation of novel flow field plate geometry for proton exchange membrane fuel cells". In: *Heat Mass Transfer* 52.10 (Oct. 2016), pp. 2167–2176. ISSN: 1432-1181. DOI: 10.1007/s00231-015-1737-6.

[13] A. P. Manso et al. "Influence of geometric parameters of the flow fields on the performance of a PEM fuel cell. A review". In: *Int. J. Hydrogen Energy* 37.20 (Oct. 2012), pp. 15256–15287. ISSN: 0360-3199. DOI: 10.1016/j.ijhydene.2012.07.076.

[14] Chao Wang et al. "The respective effect of under-rib convection and pressure drop of flow fields on the performance of PEM fuel cells". In: *Sci. Rep.* 7.43447 (Mar. 2017), pp. 1–9. ISSN: 2045-2322. DOI: 10.1038/srep43447.

[15] D. J. Ludlow et al. "PEM fuel cell membrane hydration measurement by neutron imaging". In: *J. Power Sources* 162.1 (Nov. 2006), pp. 271–278. ISSN: 0378-7753. DOI: 10.1016/j.jpowsour.2006.06.068.

[16] Tao Zeng et al. "Enhancing reactant mass transfer inside fuel cells to improve dynamic performance via intelligent hydrogen pressure control". In: *Energy* 230 (Sept. 2021), p. 120620. ISSN: 0360-5442. DOI: 10.1016/j.energy.2021.120620.

[17] Jay B. Benziger et al. "The power performance curve for engineering analysis of fuel cells". In: *J. Power Sources* 155.2 (Apr. 2006), pp. 272–285. ISSN: 0378-7753. DOI: 10.1016/j.jpowsour.2005.05.049.

[18] Eduard Marušić-Paloka and Igor Pažanin. "Effects of boundary roughness and inertia on the fluid flow through a corrugated pipe and the formula for the Darcy–Weisbach friction coefficient". In: *Int. J. Eng. Sci.* 152 (July 2020), p. 103293. ISSN: 0020-7225. DOI: 10.1016/j.ijengsci.2020.103293.

A   Complete Results
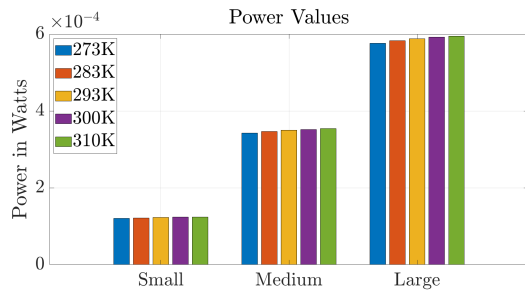
A.1   Pressure simulation results
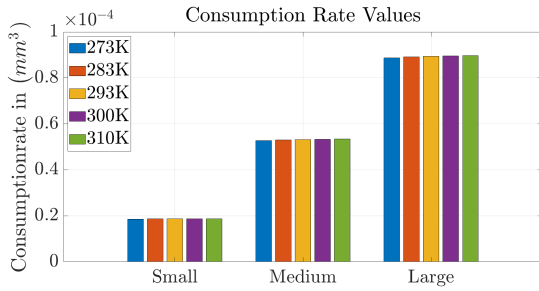
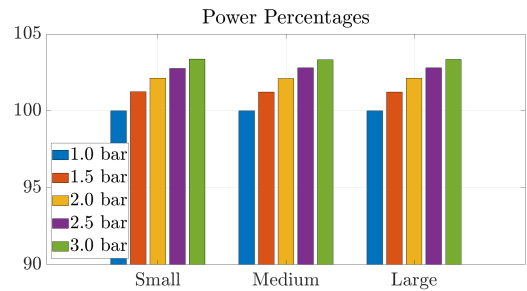(a) *Values of the consumption rate of CaH_2 when the pressure is increased, plotted for the three different sizes*
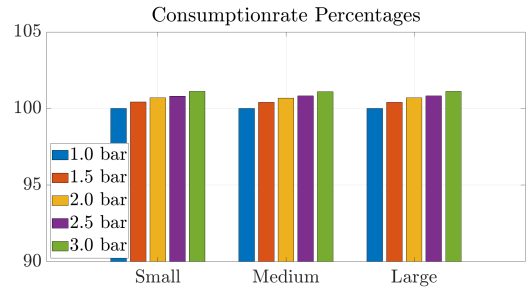
(b) *Values for the consumption rate of CaH_2 normalized against the values for 1.0 bar pressure, plotted for the three different sizes*

Figure 16: *Consumptionrates for CaH_2 for different pressures for all three sizes. Based on the model proposed by Van Renselaar et al.* [5]
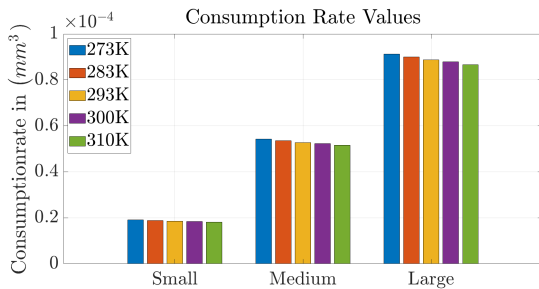

(a) *Values of the power output when the pressure is increased, plotted for the three different sizes*
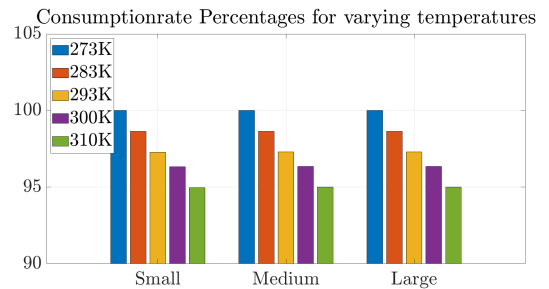

(b) *Values for the power output normalized against the values for 1.0 bar pressure, plotted for the three different sizes*

Figure 17: *Power output for different pressures for all three sizes. Based on the model proposed by Van Renselaar et al.* [5]

A.2   Temperature simulation results

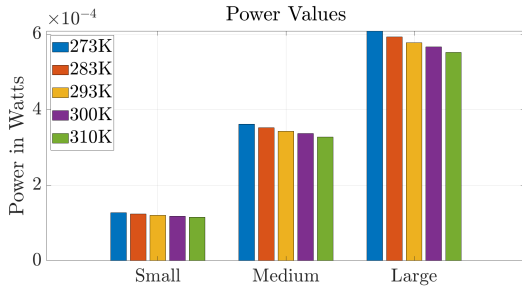(a) *Values of the consumption rate of CaH_2 when the temperature is increased, plotted for the three different sizes*
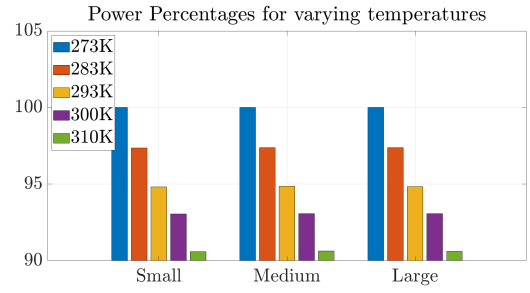

(b) *Values for the consumption rate of CaH_2 normalized against the values for 273K cell temperature, plotted for the three different sizes*

Figure 18: *Consumptionrates for CaH_2 for different temperatures for all three sizes. Based on the model proposed by Van Renselaar et al.* [5]

(a) *Values of the power output when the temperature is increased, plotted for the three different sizes*

(b) *Values for the power output normalized against the values for 273K cell temperature, plotted for the three different sizes*

Figure 19: *Power output for different cell temperatures for all three sizes. Based on the model proposed by Van Renselaar et al. [5]*

A.3 Flow trajectories

(a) *Flow in the small single serpentine plate with 1.5 bar pressure.*

(b) *Flow in the small single serpentine plate with 2.0 bar pressure.*

(c) *Flow in the small single serpentine plate with 2.5 bar pressure.*

(d) *Flow in the small single serpentine plate with 3.0 bar pressure.*

(e) *Bar of small size.*

(f) *Flow in the medium single serpentine plate with 1.5 bar pressure.*

(g) *Flow in the medium single serpentine plate with 2.0 bar pressure.*

(h) *Flow in the medium single serpentine plate with 2.5 bar pressure.*

(i) *Flow in the medium single serpentine plate with 3.0 bar pressure.*

(j) *Bar of medium size.*

(k) *Flow in the large single serpentine plate with 1.5 bar pressure.*

(l) *Flow in the large single serpentine plate with 2.0 bar pressure.*

(m) *Flow in the large single serpentine plate with 2.5 bar pressure.*

(n) *Flow in the large single serpentine plate with 3.0 bar pressure.*
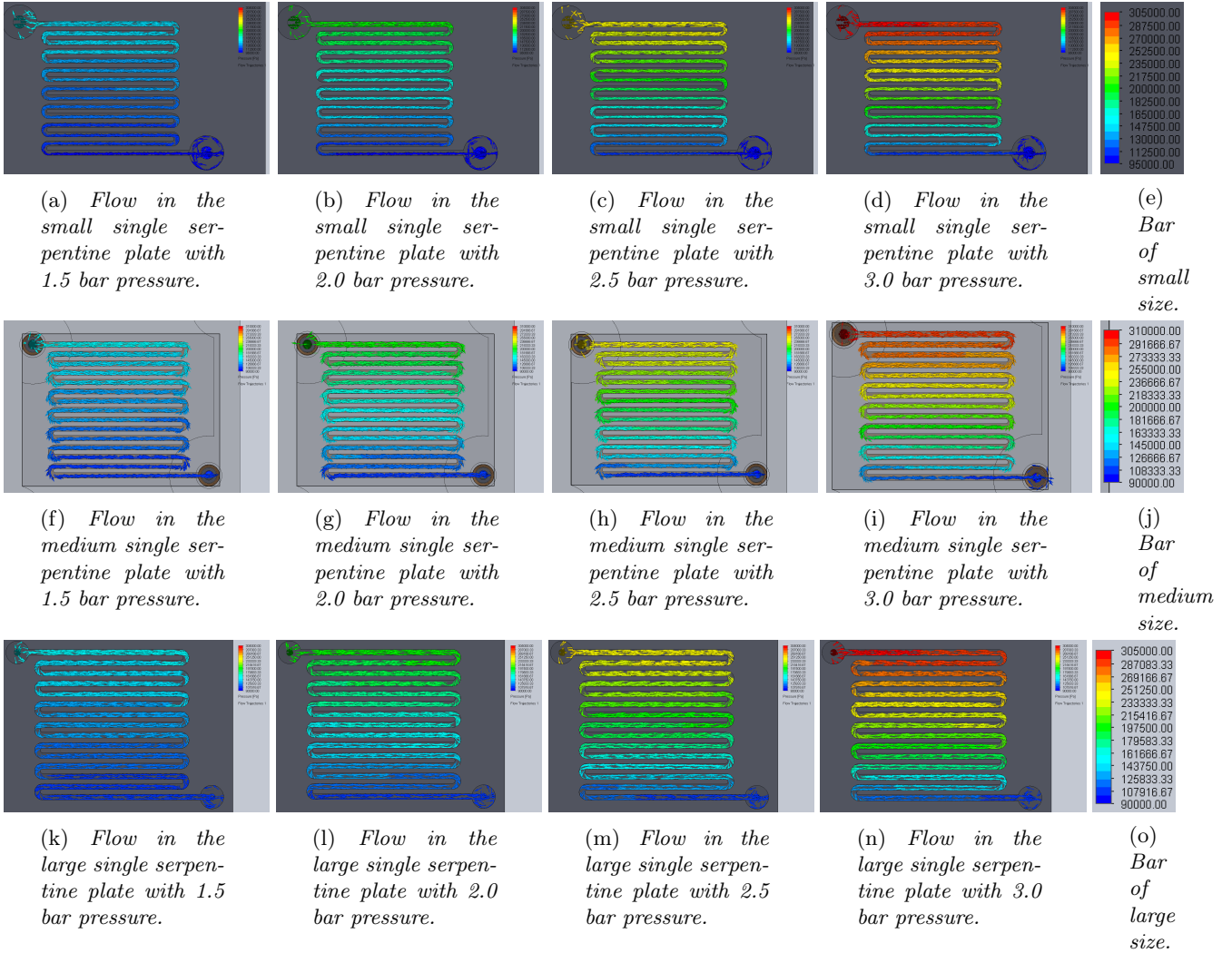
(o) *Bar of large size.*

Figure 20: *Flow simulation results of single serpentine flow plate with varying pressures and sizes. Temperature is set to 293.20K and static pressure to 101325.00 Pa. From left to right the pressure increases from 1.5 bar to 3.0 bar with steps of 0.5 bar. From top to bottom, the flow field size increases from $16 \times 16mm$ to $27 \times 27mm$ to $35 \times 35mm$. Figures 20e, 20j, and 20o show the colour scale bars for the simulations for all three sizes.*

(a) *Flow in the small 5-step plate with 1.5 bar pressure.*

(b) *Flow in the small 5-step serpentine plate with 2.0 bar pressure.*

(c) *Flow in the small 5-step serpentine plate with 2.5 bar pressure.*

(d) *Flow in the small 5-step serpentine plate with 3.0 bar pressure.*

(e) *Bar of small size.*

(f) *Flow in the medium 5-step serpentine plate with 1.5 bar pressure.*

(g) *Flow in the medium 5-step serpentine plate with 2.0 bar pressure.*

(h) *Flow in the medium 5-step serpentine plate with 2.5 bar pressure.*

(i) *Flow in the medium 5-step serpentine plate with 3.0 bar pressure.*

(j) *Bar of medium size.*

(k) *Flow in the large 5-step serpentine plate with 1.5 bar pressure.*

(l) *Flow in the large 5-step serpentine plate with 2.0 bar pressure.*

(m) *Flow in the large 5-step serpentine plate with 2.5 bar pressure.*

(n) *Flow in the large 5-step serpentine plate with 3.0 bar pressure.*
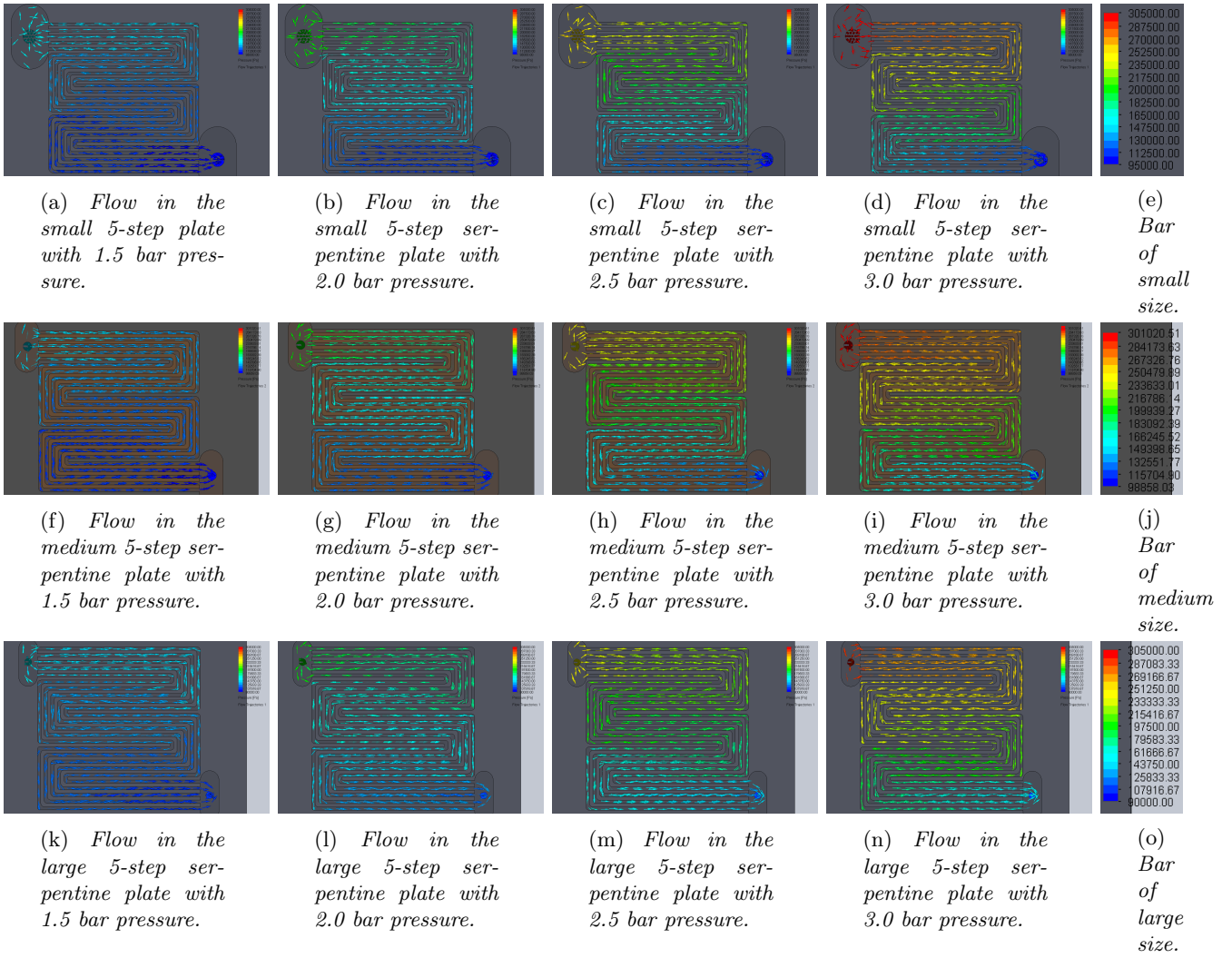
(o) *Bar of large size.*

Figure 21: *Flow simulation results of the 5-step serpentine flow plate with varying pressures and sizes. Temperature is set to 293.20K and static pressure to 101325.00 Pa. From left to right the pressure increases from 1.5 bar to 3.0 bar with steps of 0.5 bar. From top to bottom, the flow field size increases from $16 \times 16mm$ to $27 \times 27mm$ to $35 \times 35mm$. Figures 21e, 21j, and 21o show the colour scale bars of the three sizes.*

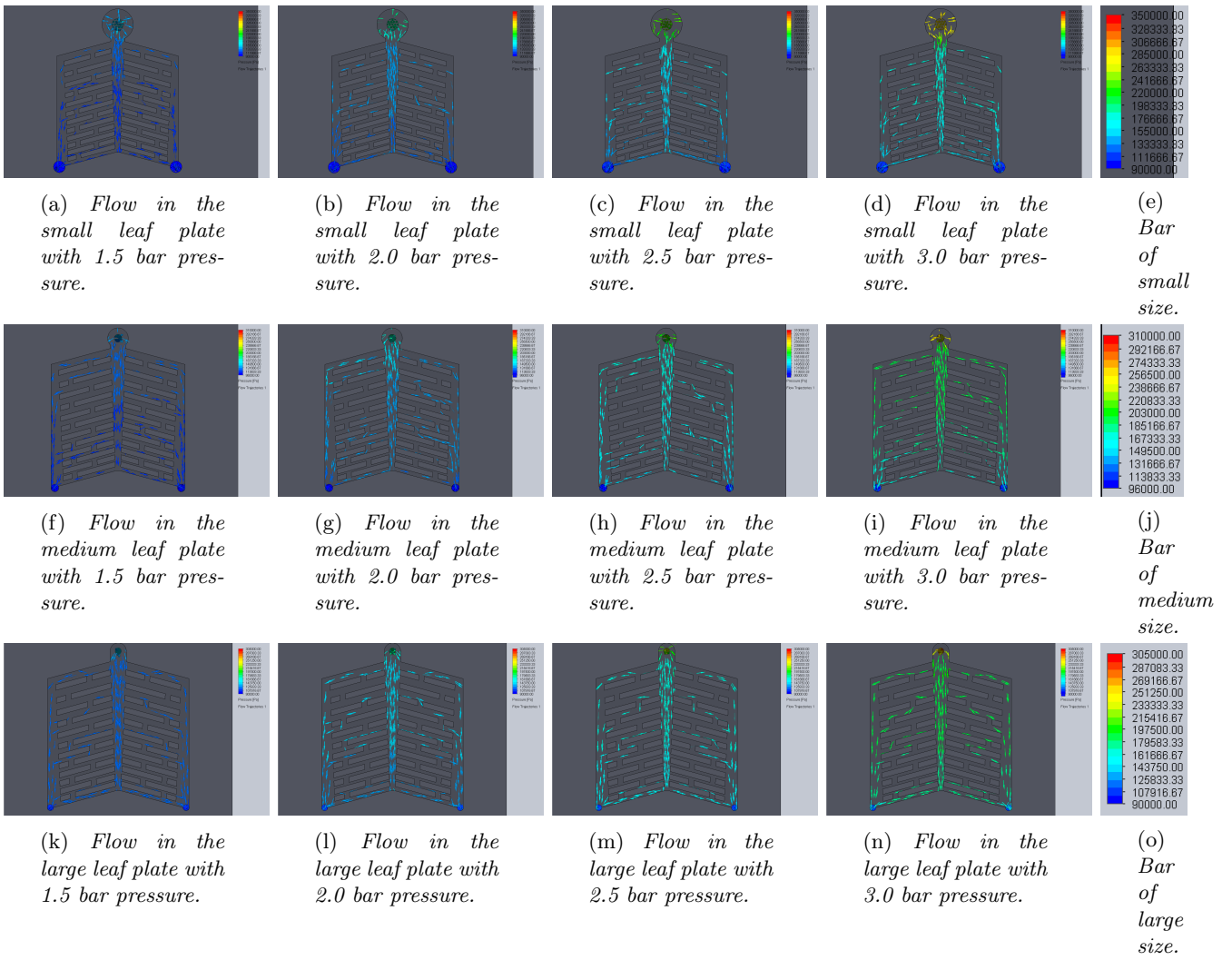(a) *Flow in the small leaf plate with 1.5 bar pressure.*

(b) *Flow in the small leaf plate with 2.0 bar pressure.*

(c) *Flow in the small leaf plate with 2.5 bar pressure.*

(d) *Flow in the small leaf plate with 3.0 bar pressure.*

(e) *Bar of small size.*

(f) *Flow in the medium leaf plate with 1.5 bar pressure.*

(g) *Flow in the medium leaf plate with 2.0 bar pressure.*

(h) *Flow in the medium leaf plate with 2.5 bar pressure.*

(i) *Flow in the medium leaf plate with 3.0 bar pressure.*

(j) *Bar of medium size.*

(k) *Flow in the large leaf plate with 1.5 bar pressure.*

(l) *Flow in the large leaf plate with 2.0 bar pressure.*

(m) *Flow in the large leaf plate with 2.5 bar pressure.*

(n) *Flow in the large leaf plate with 3.0 bar pressure.*

(o) *Bar of large size.*

Figure 22: *Flow simulation results of leaf flow plate with varying pressures and sizes. Temperature is set to 293.20K and static pressure to 101325.00 Pa. From left to right the pressure increases from 1.5 bar to 3.0 bar with steps of 0.5 bar. From top to bottom, the flow field size increases from $16 \times 16mm$ to $27 \times 27mm$ to $35 \times 35mm$. Figures 22e, 22j, and 22o show the colour scale bars of the three sizes.*
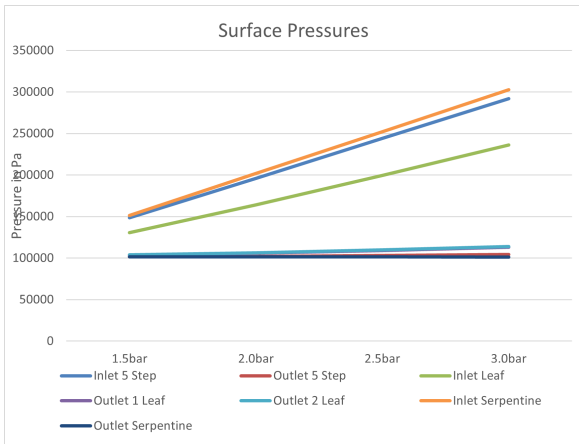
(a) *Inlet and Outlet pressures plotted against the different pressures for the three different geometries.*
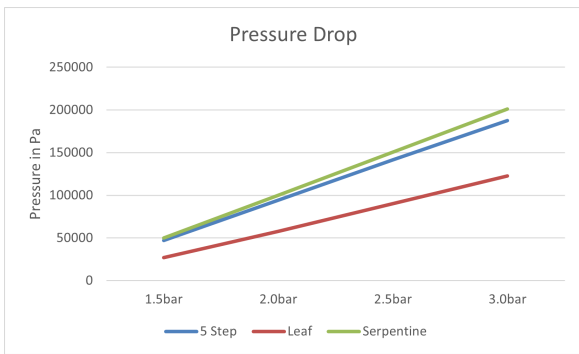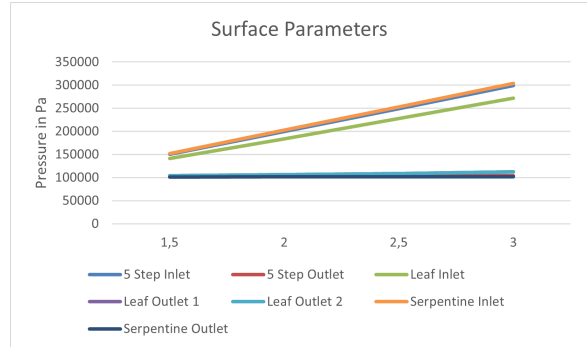

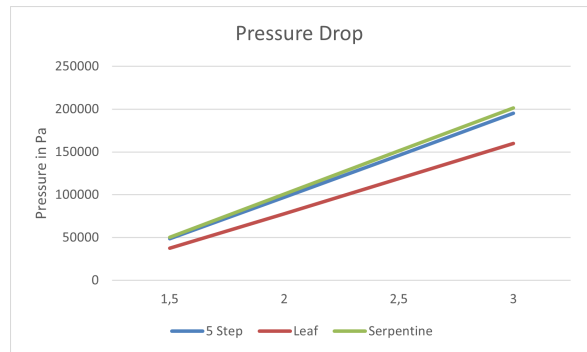(b) *Comparison of the pressure drop for the three different flow plate geometries.*
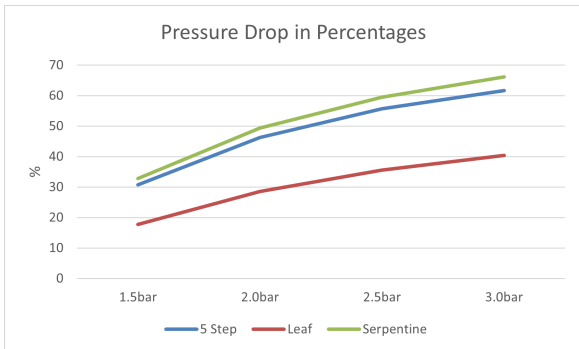
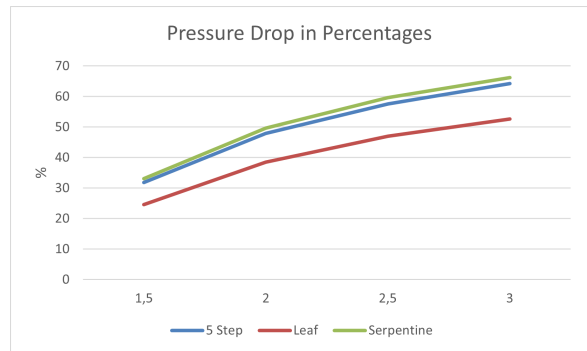(c) *Comparison of the relative pressure drop of the three different flow plate geometries.*

Figure 23: *Results of surface parameter analysis of the flow simulations with varying pressures for the medium-sized flow plates.*

(a) *Inlet and Outlet pressures plotted against the different pressures for the three different geometries.*
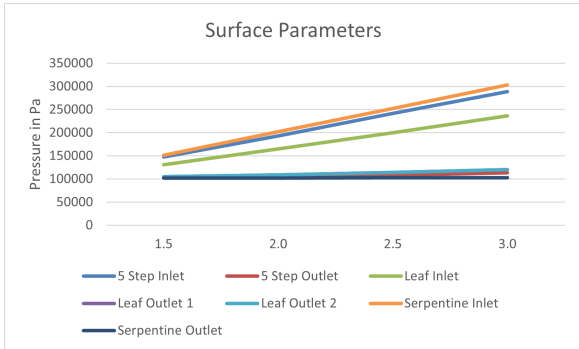

(b) *Comparison of the pressure drop for the three different flow plate geometries.*
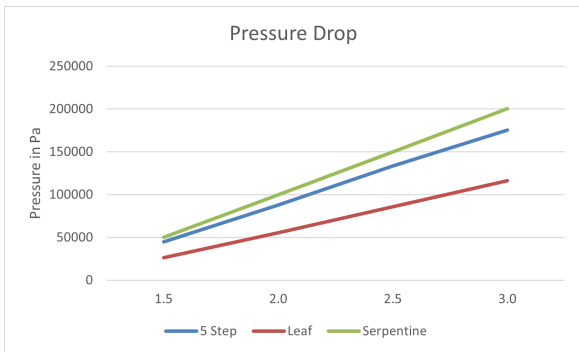

(c) *Comparison of the relative pressure drop of the three different flow plate geometries.*
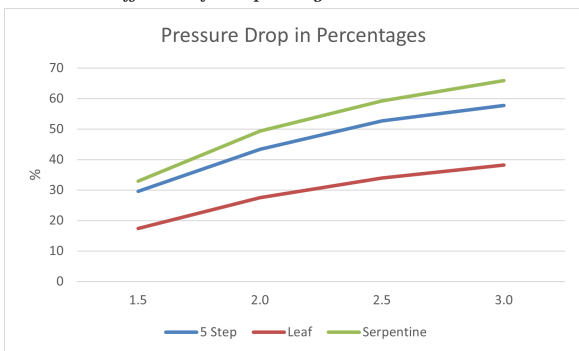
Figure 24: *Results of surface parameter analysis of the flow simulations with varying pressures for the small flow plates.*

(a) *Inlet and Outlet pressures plotted against the different pressures for the three different geometries.*

(b) *Comparison of the pressure drop for the three different flow plate geometries.*

(c) *Comparison of the relative pressure drop of the three different flow plate geometries.*

Figure 25: *Results of surface parameter analysis of the flow simulations with varying pressures for the large flow plates.*